Medical Image Analysis 55 (2019) 76–87

Contents lists available at ScienceDirect

Medical Image Analysis

journal homepage: www.elsevier.com/locate/media

Super-resolution reconstruction of neonatal brain magnetic resonance images via residual structured sparse representation

Yongqin Zhang[a,b], Pew-Thian Yap[b], Geng Chen[b], Weili Lin[b], Li Wang[b], Dinggang Shen[b,c,*]

[a] School of Information Science and Technology, Northwest University, Xi'an 710127, China
[b] Department of Radiology and BRIC, University of North Carolina at Chapel Hill, NC 27514, USA
[c] Department of Brain and Cognitive Engineering, Korea University, Seoul 136713, South Korea

ARTICLE INFO

Article history:
Received 10 July 2018
Revised 3 January 2019
Accepted 17 April 2019
Available online 18 April 2019

MSC:
68-10
62-35

Keywords:
Sparse representation
Dictionary learning
Convex optimization
Magnetic resonance imaging

ABSTRACT

Magnetic resonance images of neonates, compared with toddlers, exhibit lower signal-to-noise ratio and spatial resolution. In this paper, we propose a novel method for super-resolution reconstruction of neonate images with the help of toddler images, using residual-structured sparse representation with convex regularization. Specifically, we introduce a two-layer image representation, consisting of a *base* layer and a *detail* layer, to cater to signal variation across scanners and sites. The base layer consists of the smoothed version of the image obtained via Gaussian filtering. The detail layer is the difference between the original image and the base layer. High-frequency details in the detail layer are borrowed across subjects for super-resolution reconstruction. Experimental results on T1 and T2 images demonstrate that the proposed algorithm can recover fine anatomical structures, and generally outperform the state-of-the-art methods both qualitatively and quantitatively.

1. Introduction

Magnetic resonance imaging (MRI), due to its excellent soft tissue contrast, is useful in assisting pediatric doctors in diagnosis, prognosis, and treatment planning of newborns affected by neurodisorders. However, this technique is often not optimized for imaging pediatric subjects. Hardware and software developed for adults are often directly applied to pediatric subjects with little modifications. In neonatal images, partial volume effect (PVE) causes blurred tissue boundaries, where a single voxel may contain signals from several tissue types. This poses challenges in quantitative analysis of magnetic resonance (MR) images. To decrease PVE, the common strategy is to use smaller-defined voxels for image acquisition. Although this strategy can capture more details with higher spatial resolution, it also causes lower signal-to-noise ratio (SNR) and longer scan time. In practice, the neonatal images are usually notably noisy and blurred with low resolution due to the small brain size, brain immaturity and non-optimized MRI scanners. However, high-resolution (HR), rather than low-resolution (LR), images are desired in MR applications. In this paper, we will introduce a super-resolution (SR) technique (Yue et al., 2016) to reconstruct HR images from one or more LR images.

1.1. Early methods

Image interpolation (Lehmann et al., 1999; Huang et al., 2015) is commonly used to construct the unknown data points on the regular grids of an HR image from known data points of an LR image. Typical interpolation methods include polynomial interpolation, spline interpolation, and edge-directed interpolation. Although these interpolation methods have low computational costs, they often over-smooth images and cause edge halos. Moreover, these methods merely perform weighted averaging on neighboring voxels without considering the image degradation process and thus cannot recover high-frequency details of the HR images.

1.2. Contemporary SR methods

Unlike interpolation, contemporary SR methods use knowledge of image degradation and image priors in recovering HR images. Image SR problems are generally ill-posed and need to be regularized so that reasonable solutions can be obtained. The regularization terms are commonly constructed via image priors imposed based on edge statistics (Fattal, 2007), image gradients (Krishnan and Fergus, 2009; Sun et al., 2011; Yan et al., 2015; Yao et al., 2018;

* Corresponding author at: Department of Radiology and BRIC, University of North Carolina at Chapel Hill, NC 27514, USA.
E-mail address: dgshen@med.unc.edu (D. Shen).

https://doi.org/10.1016/j.media.2019.04.010
1361-8415/

Zhu et al., 2018), self-similarity (Buades et al., 2005; Zhang et al., 2012a; 2014), and/or sparsity (Candes et al., 2008; Yu et al., 2012; Dong et al., 2013; Zhang et al., 2015a,b).

Aly and Dubois (2005) introduced an image up-sampling method using total-variation (TV) regularization. Osher and his colleagues (Marquina and Osher, 2008) proposed the Bregman iteration algorithm to solve TV-based image SR problems. By modeling the shape of image gradients, Sun et al. (2011) presented an image SR approach based on the gradient profile learned from a large number of natural images. Recently, using global and local image information, Shi et al. (2015) presented an image SR reconstruction approach with low-rank and TV regularization. But TV-based approaches tend to over-smooth HR images due to its piecewise constant assumption.

Manjon et al. (2010) proposed a nonlocal upsampling (NLMU) method by exploiting structural self-similarity. Rousseau and ADNI (Rousseau and Initiative, 2010) proposed an example-based SR method with nonlocal regularization for the resolution enhancement of a single LR image under the guidance of an HR image. Yang et al. (2010) presented a single image SR method based on coupled dictionaries trained from LR and HR image patch pairs. By exploiting the image gradient distribution and the image structural self-similarity in both scale domain and spatial domain, Zhang et al. (2015a) proposed an image SR method based on the structure-constrained sparse representation. Hou et al. (2018) presented an adaptive SR method based on sparse representation with global joint dictionary model. These SR methods mainly focus on imposing natural image priors to regularize the solutions to the ill-posed inverse problems.

Recently, deep learning-based SR methods show impressive results in the fields of image processing and computer vision. Dong et al. (2016) presented a deep learning method via a deep convolutional neural network (CNN) for single image SR. Mao et al. (2016) proposed skip connections to symmetrically link convolutional and deconvolutional layers to achieve training convergence acceleration and a higher-quality local optimum. Ledig et al. (2017) proposed a generative adversarial network for photo-realistic image SR by a united framework of an adversarial loss and a content loss. Tai et al. (2017) presented a deep recursive residual network by residual learning in global and local manners. Pham et al. (2017a) introduced a three-dimensional (3D) CNN model for brain MR image SR, and then extended it to multimodal SR (Pham et al., 2017b). Chen et al. (2018b) presented a 3D densely connected SR network to restore high-resolution features of structural brain MR images, and subsequently extended it to a multi-level version (Chen et al., 2018a) by training a generative adversarial network. However, these SR methods did not consider the discrepancies between test and training images, and directly learn the priors from a large dataset with deep learning models to improve the quality of SR. In our case, we do not have enough training data for SR reconstruction of neonatal images.

Although existing SR methods are reasonably effective, they mostly use convex regularization. Nonconvex regularizations are shown to provide better solutions to image SR problems (Tuia et al., 2016; Liu et al., 2016). Furthermore, all existing SR methods almost deal with natural images (Dong et al., 2016; Mao et al., 2016; Ledig et al., 2017; Tai et al., 2017) or adult images (Pham et al., 2017a,b; Chen et al., 2018a,b), but rarely process neonatal MR images, which typically have very low spatial resolution with severe partial volume effect and heavy noise.

1.3. Main contributions

In this paper, we propose a novel method for SR reconstruction of the MR image of a neonate with the help of MR images of toddlers, using residual-structured sparse representation with convex regularization. Our contribution is threefold: (1) We incorporate high-frequency information from toddler images as priors in the form of dictionaries; (2) We incorporate a partly quadratic nonconvex regularization for SR reconstruction of neonatal images; and (3) We harness nonlocal structural self-similarity for enhancing structured sparse representation.

1.4. Organization

The rest of this paper is organized as follows. In Section 2, we provide information on model-based SR reconstruction. In Section 3, we flesh out our SR method, which incorporates a longitudinal prior and convex regularization, and the optimization scheme using alternating minimization. In Section 4, we report extensive experimental results. In Section 5, we give relevant discussions on using our method for neonatal SR. In Section 6, we draw conclusions.

2. Background

2.1. Image degradation model

The degradation process of an observed LR image from an HR image is generally modeled as

$$\mathbf{Y} = \mathbf{HX} + \boldsymbol{\upsilon}, \tag{1}$$

where $\mathbf{Y}$ is the observed LR image, $\mathbf{X}$ is the original HR image, $\mathbf{H}$ is the degradation matrix associated with blurring and downsampling, and $\boldsymbol{\upsilon}$ is the Gaussian noise. Since different HR images could degenerate into the same set of LR images, image SR aims to infer an appropriate HR image from one or multiple LR image(s) by solving an ill-posed inverse problem with the help of regularization.

2.2. Sparse representation

The key idea of sparse representation is to decompose a signal as a linear combination of only a few atoms in an over-complete dictionary. According to the sparse representation theory, the sparse decomposition of an image $\mathbf{X}$ is formulated as follows:

$$\left(\hat{\mathbf{D}}, \boldsymbol{\alpha}_{\mathbf{X}}\right) = \arg\min_{\mathbf{D},\boldsymbol{\alpha}} \|\boldsymbol{\alpha}\|_0, \quad \text{s.t.} \quad \mathbf{X} = \mathbf{D}\boldsymbol{\alpha}, \tag{2}$$

where $\boldsymbol{\alpha}$ is the sparse matrix, $\|\boldsymbol{\alpha}\|_0$ is the ℓ_0 pseudo-norm counting the number of non-zero components of $\boldsymbol{\alpha}$, and $\mathbf{D} \in \mathbb{R}^{p^3 \times \kappa}$ ($p^3 \ll \kappa$) is an over-complete dictionary. Since Eq. (2) is typically an NP-hard problem, it is relaxed as a convex optimization problem by using the ℓ_1 norm instead. Eq. (2) can be relaxed in the following form:

$$\left(\hat{\mathbf{D}}, \boldsymbol{\alpha}_{\mathbf{X}}\right) = \arg\min_{\mathbf{D},\boldsymbol{\alpha}} \|\mathbf{X} - \mathbf{D}\boldsymbol{\alpha}\|_2^2 + \lambda\|\boldsymbol{\alpha}\|_1, \tag{3}$$

where $\|\boldsymbol{\alpha}\|_1$ is the sparsity-inducing ℓ_1 regularization term, and λ is a penalty parameter.

Since the observation $\mathbf{Y}$ of $\mathbf{X}$ is often blurred and noisy according to Eq. (1), sparse modeling of image SR can be expressed as follows:

$$\left(\hat{\mathbf{D}}, \boldsymbol{\alpha}_{\mathbf{Y}}\right) = \arg\min_{\mathbf{D},\boldsymbol{\alpha}} \|\mathbf{Y} - \mathbf{HX}\|_2^2 + \lambda\|\boldsymbol{\alpha}\|_1, \quad \text{s.t.} \quad \mathbf{X} = \mathbf{D}\boldsymbol{\alpha}. \tag{4}$$

Ideally, $\boldsymbol{\alpha}_{\mathbf{Y}}$ should be sufficiently close to $\boldsymbol{\alpha}_{\mathbf{X}}$. The solution to Eq. (4) is given by the least absolute shrinkage and selection operator (LASSO) (Tibshirani, 1996). LASSO corresponds to the

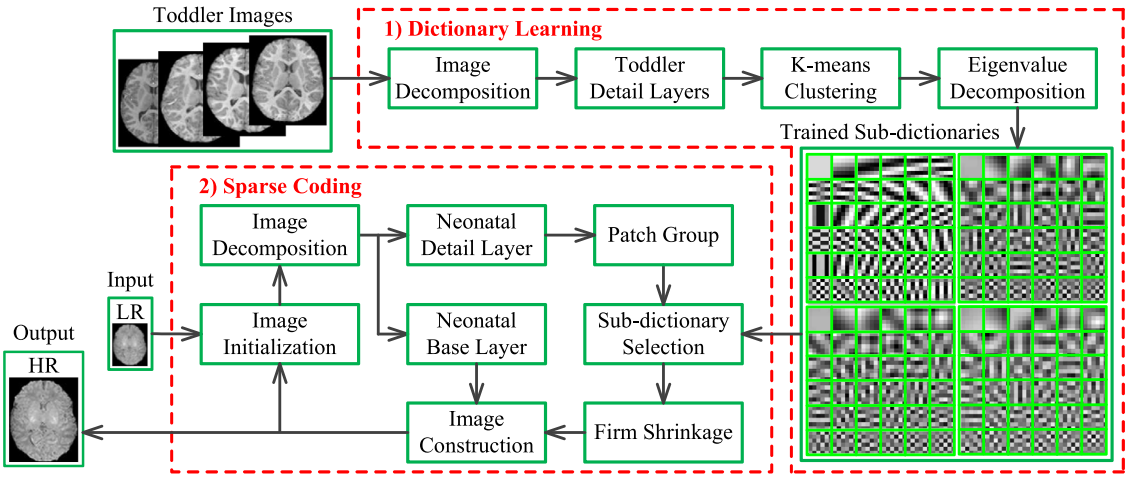

Fig. 1. Overview of the proposed method.

maximum a posteriori (MAP) estimation of the sparse coefficients with a Laplace distribution prior (Park and Casella, 2008):

$$f(\alpha_{i,j}|\theta_{i,j}) = \frac{1}{2\theta_{i,j}} \exp\left(-\frac{|\alpha_{i,j}|}{\theta_{i,j}}\right). \tag{5}$$

Here $\alpha_{i,j}$ is the (i, j)th entry of the sparse matrix $\boldsymbol{\alpha}$, and $\theta_{i,j}$ is the standard deviation of $\alpha_{i,j}$. According to Bayesian MAP estimation theory, the penalty parameter in Eq. (4) can be derived as $\lambda_{i,j} = 2\sigma_v^2/\theta_{i,j}$, where σ_v^2 is the variance of the approximation errors.

Over the past more than ten years, sparse representation and dictionary learning have been widely used in medical image analysis (Lustig et al., 2007; 2008; Zhang et al., 2012b,c; Su et al., 2015; Jiang et al., 2018). However, they rarely involve SR reconstruction of neonatal images. In our previous work, we proposed a low-rank and total variation (LRTV) method (Shi et al., 2015) and then generalized it to LGSR (Zhang et al., 2018) for neonatal image SR using longitudinal data of the same subject. In this paper, we propose a sparse representation method to infer the appropriate HR images from neonatal LR images using longitudinal data of different subjects.

3. Method

3.1. Residual-structured sparse representation (RSSR)

In this work, let the LR images denote the low-quality neonatal images acquired by MRI scanners, whereas the HR images represent the desired high-quality neonatal MR images. Fig. 1 is an overview of the proposed method. First, the detail layers are extracted from the images of multiple toddlers using image decomposition. All 3D patches in the detail layers are separated into K clusters with the corresponding cluster centers by k-means clustering. These clusters are used to train the sub-dictionaries beforehand (see Section 3.2) for iterative reconstruction of the HR image. Then an initial estimate of the HR image is obtained from the LR neonatal image via spline interpolation. In each iteration, the HR image is decomposed into the base layer and the detail layer. The detail layer is refined by reconstructing each patch in the layer via sparse coding over an appropriate pre-learned sub-dictionary. Finally, the reconstructed detail layer is then added to the base layer to reconstruct the refined HR image. In what follows, we will flesh out the details of this approach, which we call residual-structured sparse representation (RSSR).

From an observed LR neonatal image $\mathbf{Y}$, we reconstruct the corresponding HR neonatal image $\mathbf{X}$, with a longitudinal prior, by minimizing the following objective function:

$$\begin{aligned}\left(\hat{\mathbf{X}}, \mathbf{D}_\mathbf{L}, \boldsymbol{\alpha}_\mathbf{Y}\right) = \arg\min_{\mathbf{X},\mathbf{D},\boldsymbol{\alpha}} \|\mathbf{Y} - \mathbf{H}\mathbf{X}\|_2^2 + \lambda \sum_i \|\boldsymbol{\alpha}_i - \boldsymbol{\mu}_i\|_1, \\ \text{s.t.} \quad \mathbf{X} = \mathbf{Z} + \mathbf{E}, \quad \mathbf{E} = \mathbf{D}\boldsymbol{\alpha},\end{aligned} \tag{6}$$

where $\mathbf{X}$ is decomposed into the base layer $\mathbf{Z}$ and the detail layer $\mathbf{E}$ using Gaussian filtering, $\mathbf{D}$ is the pre-learned dictionary trained from the detail layers of N toddler images denoted by $\mathbf{L} = (\mathbf{L}_1, \mathbf{L}_2, \cdots, \mathbf{L}_N)$, $\mathbf{H}$ is the degradation matrix, $\boldsymbol{\alpha}_i$ is the sparse code of a patch $\mathbf{E}_i$ centered at position i in the detail layer $\mathbf{E}$, and $\boldsymbol{\mu}_i$ is the weighted average of sparse codes $\boldsymbol{\alpha}_g$ of similar patches $\mathbf{E}_g$ associated with patch $\mathbf{E}_i$ in the detail layer $\mathbf{E}$. Specifically, $\boldsymbol{\mu}_i$ is given by

$$\boldsymbol{\mu}_i = \frac{1}{W} \sum_{g \in \Omega_i} w_{i,g} \boldsymbol{\alpha}_g, \tag{7}$$

where $w_{i,g} = \exp(-\|\boldsymbol{\alpha}_g - \boldsymbol{\alpha}_i\|_2^2/h)$ with the decay-rate parameter h, and the normalization factor $W = \sum_g w_{i,g}$. Since image SR aims to recover the high-frequency details, we assume that the base layer $\mathbf{Z}$ of HR image is the same as that of LR image. To solve problem (6), we will first train the dictionary $\mathbf{D}$ offline from a set of toddler images $\mathbf{L}$ and then compute the sparse codes $\boldsymbol{\alpha}$ to estimate the HR neonatal image $\mathbf{X}$.

We generalize the ℓ_1 norm regularization term in Eq. (6) to a parameterized nonconvex regularization term and rewrite the objective function as follows:

$$\begin{aligned}\left(\hat{\mathbf{X}}, \mathbf{D}_\mathbf{L}, \boldsymbol{\alpha}_\mathbf{Y}\right) = \arg\min_{\mathbf{X},\mathbf{D},\boldsymbol{\alpha}} \|\mathbf{Y} - \mathbf{H}\mathbf{X}\|_2^2 + \lambda \sum_i \Phi(\boldsymbol{\alpha}_i; c), \\ \text{s.t.} \quad \mathbf{X} = \mathbf{Z} + \mathbf{E}, \quad \mathbf{E} = \mathbf{D}\boldsymbol{\alpha},\end{aligned} \tag{8}$$

where $c \geq 0$ is a tuning parameter for the nonconvex regularization term Φ. Here we propose to define Φ using a partly quadratic penalty (PQP) function:

$$\Phi(\boldsymbol{\alpha}_i; c) = \begin{cases} \|\boldsymbol{\alpha}_i - \boldsymbol{\mu}_i\|_1 - \frac{c}{2}\|\boldsymbol{\alpha}_i - \boldsymbol{\mu}_i\|_2^2, & \|\boldsymbol{\alpha}_i - \boldsymbol{\mu}_i\|_1 < \frac{1}{c}, \\ \frac{1}{2c}, & \|\boldsymbol{\alpha}_i - \boldsymbol{\mu}_i\|_1 \geqslant \frac{1}{c}. \end{cases} \tag{9}$$

By saturating strong signals and keeping weak signals relatively unchanged, the PQP function provides good contrast between strong and weak signals. We will derive a convex solution to problem (8).

3.2. Algorithm of RSSR

To estimate the HR neonatal image from an LR input, we can break down the optimization problem (8) into two sub-problems: (1) Dictionary learning and (2) Sparse coding.

(1) Dictionary Learning

Images from N toddlers are used to learn the dictionary for neonatal image SR. Each toddler image is decomposed by Gaussian filtering to obtain the base and detail layers. We sample the small patches of size $p \times p \times p$ centered at each pixel in the detail layers. All these patches of detail layers are partitioned into K clusters, using k-means clustering by minimizing the sum of squares distances between the patches in a cluster with the cluster center. The objective function of k-means clustering is defined as

$$\hat{\mathbf{B}} = \arg\min_{\mathbf{B}} \sum_{k=1}^{K} \sum_{\mathbf{b}\in\mathbf{B}_k} \|\mathbf{b} - \mathbf{m}_k\|^2, \tag{10}$$

where K is the number of clusters, $\mathbf{B} = \{\mathbf{B}_1, \mathbf{B}_2, \cdots, \mathbf{B}_K\}$ is the set of patch clusters, $\mathbf{m}_k$ is the center of the kth cluster $\mathbf{B}_k$, and $\mathbf{b}$ denotes an image patch in the detail layers $\mathbf{R}$ extracted from toddler images $\mathbf{L} = (\mathbf{L}_1, \mathbf{L}_2, \cdots, \mathbf{L}_N)$. An efficient heuristic iterative approach with fast local convergence is commonly used to solve problem (10). For each optimized cluster $\hat{\mathbf{B}}_k$, we compute the covariance matrix $\hat{\mathbf{B}}_k\hat{\mathbf{B}}_k^T$ and then perform eigenvalue decomposition on $\hat{\mathbf{B}}_k\hat{\mathbf{B}}_k^T$, where each column of $\hat{\mathbf{B}}_k$ is a patch. The eigenvectors form the corresponding sub-dictionary $\mathbf{D}_k$:

$$\mathbf{D}_k = \left\{\mathbf{d} : \left(\hat{\mathbf{B}}_k\hat{\mathbf{B}}_k^T - \beta\mathbf{I}\right)\mathbf{d} = 0\right\}, \tag{11}$$

where $\mathbf{d}$ is an eigenvector with eigenvalue β, and $\mathbf{I}$ is an identity matrix. The sub-dictionaries are collected in $\mathbf{D}_\mathbf{L} = \{\mathbf{D}_1, \mathbf{D}_2, \cdots, \mathbf{D}_K\}$.

(2) Sparse Coding

By fixing the dictionary $\mathbf{D}_\mathbf{L} = \{\mathbf{D}_1, \mathbf{D}_2, \cdots, \mathbf{D}_K\}$, the minimization problem (8) can be reduced to

$$\begin{aligned}\left(\hat{\mathbf{X}}, \boldsymbol{\alpha}_\mathbf{Y}\right) = \arg\min_{\mathbf{X},\boldsymbol{\alpha}} \|\mathbf{Y} - \mathbf{H}\mathbf{X}\|_2^2 + \sum_{i,k} \lambda_{i,k}\Phi\left(\boldsymbol{\alpha}_{i,k}; c\right),\\ \text{s.t.} \quad \mathbf{X} = \mathbf{Z} + \mathbf{E}, \quad \mathbf{E} = \mathbf{D}_\mathbf{L}\boldsymbol{\alpha}.\end{aligned} \tag{12}$$

Lemma 1:*If $\lambda > 0$ and $0 \le c < 1/\lambda$, then the objective function in Eq. (12) is strictly convex (Gao and Bruce, 1997; Bayram, 2016).*

We use an iterative shrinkage algorithm (Bioucas-Dias and Figueiredo, 2007; Beck and Teboulle, 2009) to solve the sparse coding problem (12). In each iteration t, by keeping $\boldsymbol{\mu}_i^{(t)}$ fixed, we derive a convergent analytical solution to update the sparse codes $\boldsymbol{\alpha}_{i,k}^{(t+1)}$ as follows:

$$\boldsymbol{\alpha}_{i,k}^{(t+1)} = \mathcal{S}_{\eta/c}\left(\boldsymbol{\gamma}_{i,k}^{(t)}, \boldsymbol{\lambda}_{i,k}^{(t)}\right) + \boldsymbol{\mu}_{i,k}^{(t)}, \tag{13}$$

$$\boldsymbol{\gamma}^{(t)} = \boldsymbol{\alpha}^{(t)} - \boldsymbol{\mu}^{(t)} + \eta\mathbf{D}_\mathbf{L}^T\mathbf{H}^T\left(\mathbf{Y} - \mathbf{H}\left(\mathbf{Z}^{(t)} + \mathbf{D}_\mathbf{L}\boldsymbol{\alpha}^{(t)}\right)\right), \tag{14}$$

with the proximal operator $\mathcal{S}_{\eta/c}(u, v)$ defined as

$$\mathcal{S}_{\eta/c}(u, v) = \min\left\{|u|, \max\left(|u| - \eta v\right)/(1 - c\eta v), 0\right\}\operatorname{sign}(u), \tag{15}$$

where $\operatorname{sign}(\cdot)$ is the signum function, and η is an auxiliary parameter ensuring the convergence of the iterative shrinkage algorithm. The iterative shrinkage solution (13) is a proximal operator applied to $\boldsymbol{\gamma}^{(t)}$ by the element-wise thresholding. This deduced proximal operator $\mathcal{S}_{\eta/c}$ also has the same form as the firm threshold function (Gao and Bruce, 1997). In the process of sparse coding, we first decompose the current estimated HR neonatal image $\mathbf{X}^{(t)}$ into the base layer $\mathbf{Z}^{(t)}$ and the detail layer $\mathbf{E}^{(t)}$. Then we update $\mathbf{E}^{(t)}$ and compute the sparse codes $\boldsymbol{\alpha}_i^{(t)}$ of each patch $\mathbf{e}_i^{(t)}$ in the detail layer by selecting an appropriate trained sub-dictionary $\mathbf{D}_k$ with the minimal Euclidean distance between the patch $\mathbf{e}_i^{(t)}$ and the corresponding cluster center $\mathbf{m}_k$ among K cluster centers. Next, we separately update the nonlocal mean $\boldsymbol{\mu}^{(t)}$ of $\boldsymbol{\alpha}^{(t)}$ and the regularization parameter $\boldsymbol{\lambda}_{i,k}^{(t)} = 2\delta^{(t)}/\boldsymbol{\theta}_{i,k}^{(t)}$ with the sparse codes $\boldsymbol{\alpha}^{(t)}$, where $\delta^{(t)}$ and $\boldsymbol{\theta}_{i,k}^{(t)}$ are separately the noise variance of the estimated HR image $\hat{\mathbf{X}}^{(t)}$ and the standard deviation of the sparse codes $\boldsymbol{\alpha}_{i,k}^{(t)}$. After that, the sparse codes $\boldsymbol{\alpha}_{i,k}^{(t)}$ are updated to $\boldsymbol{\alpha}_{i,k}^{(t+1)}$ by the iterative shrinkage function in Eq. (13). Later, we update the HR neonatal image estimate $\mathbf{X}^{(t+1)}$ by adding the base layer $\mathbf{Z}^{(t)}$ and the super-resolved detail layer $\mathbf{D}_\mathbf{L}\boldsymbol{\alpha}^{(t+1)}$. This above iterative process of sparse coding proceeds until the convergence (e.g., the maximum number T_0 of iterations) is reached (Bayram, 2016). Finally, we get the estimated HR neonatal image $\hat{\mathbf{X}}$. The proposed RSSR algorithm is summarized in Algorithm 1.

Algorithm 1 Pseudocode of the RSSR Algorithm.

Input: LR neonatal image $\mathbf{Y}$, a scaling factor s and a set of toddler images $\mathbf{L} = \{L_1, \cdots, L_N\}$.

Output: Estimated HR neonatal image $\hat{\mathbf{X}}$.

I. Initialize the parameters λ, K, ρ and c;

II. Offline dictionary learning:

- Partition toddler images $\mathbf{L}$ into base layers and detail layers $\mathbf{R}$;
- Cluster the patches of $\mathbf{R}$ into K clusters using Eq. (10);
- Eigendecompose the covariance matrix of each cluster to construct a sub-dictionary $\mathbf{D}_k$;
- Collect all sub-dictionaries $\{\mathbf{D}_k\}$ in $\mathbf{D}_\mathbf{L}$;

III. Initialize the HR image $\mathbf{X}$ by spline interpolation;

IV. Sparse coding: **while** (not convergence) **do**

- Partition $\mathbf{X}^{(t)}$ into the base layer $\mathbf{Z}^{(t)}$ and the detail layer $\mathbf{E}^{(t)}$;
- Update $\mathbf{E}^{(t)} = \mathbf{E}^{(t)} + \rho\mathbf{H}^T\left(\mathbf{Y} - \mathbf{H}\mathbf{X}^{(t)}\right)$;
- Calculate sparse codes $\boldsymbol{\alpha}_{i,k}^{(t)} = \mathbf{D}_k^T\mathbf{e}_i^{(t)}$ of $\mathbf{e}^{(t)}$ in the detail layer $\mathbf{E}^{(t)}$ by choosing an appropriate trained sub-dictionary $\mathbf{D}_k$;
- Compute the nonlocal mean $\boldsymbol{\mu}^{(t)}$ of $\boldsymbol{\alpha}^{(t)}$, η and λ;
- Update sparse codes $\boldsymbol{\alpha}_{i,k}^{(t+1)}$ by Eq. (13);
- Update the HR image estimate $\mathbf{X}^{(t+1)} = \mathbf{Z}^{(t)} + \mathbf{D}_\mathbf{L}\boldsymbol{\alpha}^{(t+1)}$;

end while

Return the estimated HR image $\hat{\mathbf{X}} = \mathbf{X}^{(t+1)}$.

4. Experiments

4.1. Dataset

With consent from their parents, 27 pediatric subjects participated in a large study of early brain development (Gilmore et al., 2007). This research was approved by the institutional review board (IRB) of the University of North Carolina at Chapel Hill. The first 24 subjects were scanned at birth by a 3T MRI head-only scanner (Siemens MAGNETOM Tim Trio) using a 32-channel head coil. Only the first 8 of them had a follow-up scan at 2 years of age. The other 3 subjects were scanned at multiple time points (i.e., 24, 36, 48, 60 and 72 months). For each subject, two imaging modalities were collected: A T1 image with 144 sagittal slices at the resolution of $1 \times 1 \times 1\,\text{mm}^3$ and a T2 image with 58 axial slices at the resolution of $1.25 \times 1.25 \times 1.95\,\text{mm}^3$. In the preprocessing pipeline, T2 images were resampled and then linearly registered to their corresponding T1 images. The images were bias-corrected and skull-stripped (Shi et al., 2012).

4.2. Experimental settings

The ℓ_1 norm is a special case of the partly quadratic function. This can be seen from the fact that Eq. (8) reduces to Eq. (6) when

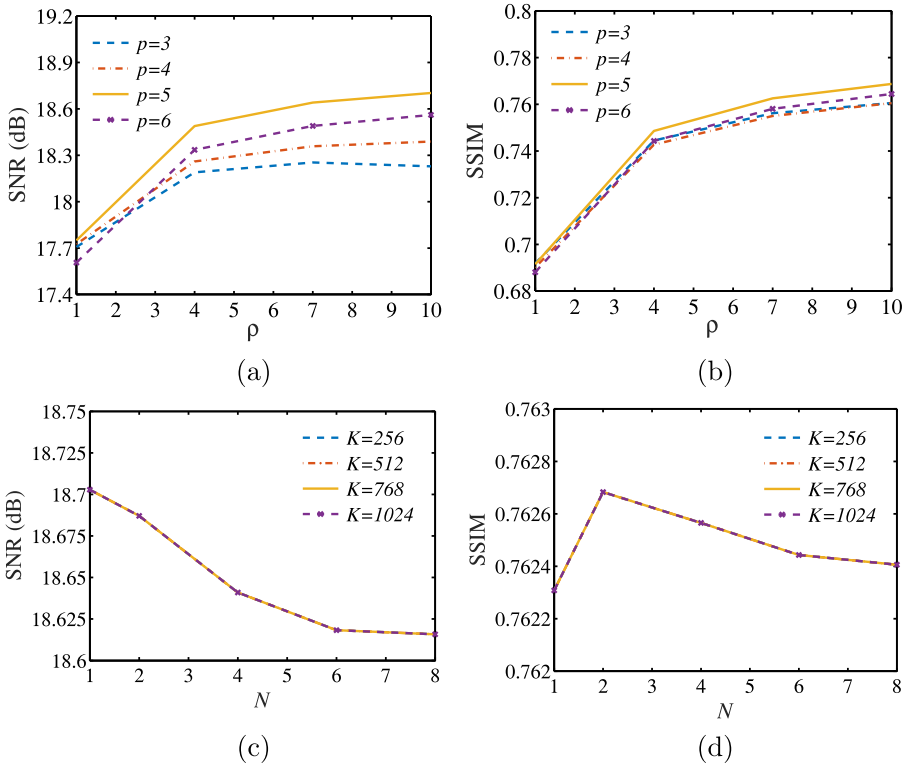

Fig. 2. SNR/SSIM values given by RSSR2 with respect to key parameters.

$c = 0$. For conciseness, we use RSSR1 to denote (6) with ℓ_1 norm regularization and RSSR2 to represent (8) with partly quadratic penalty regularization. For evaluation, we simulated a set of LR neonatal images by blurring and downsampling the original neonatal images. For blurring, we used a Gaussian kernel of size $5 \times 5 \times 5$ with a standard deviation of 1 voxel, which is different from that of LRTV (Shi et al., 2015) and LGSR (Zhang et al., 2018). We used two metrics, SNR and structural similarity index (SSIM) (Wang et al., 2004), to measure the similarity between the reconstructed HR image and the original image. In all experiments, we used an upscaling factor of 2.

In the experiments, the parameters for our method were as follows: $p = 5$, $w_s = 15$, $\rho = 7$, $c = 0.6$, $T_0 = 120$, $N = 4$, $K = 1024$, and the initial value $\delta^{(0)} = 1.8$. We analyzed the sensitivity of the proposed method to the parameters by changing one parameter while keeping the others fixed. For one sample image, Fig. 2 shows the SNR and SSIM results of the proposed method with respect to changes of the key parameters p, ρ, N and K. It can be seen from the figure that the changes in p, ρ, and N have notable impact on SNR/SSIM, whereas the changes in K have little influence on the outcome. Fig. 2(a) and (b) shows that SNR and SSIM increase as the parameter ρ increases, but a large ρ may cause the algorithm to not converge and deteriorate the reconstructed images. Fig. 2(c) and (d) indicate that SNR and SSIM decrease as the number of images N increases, and the number of sub-dictionaries K has minimal impact on SNR and SSIM (see further explanation in Section 5).

4.3. Intra- and inter-subject dictionaries

We evaluated whether toddler images of different subjects can be used for neonatal SR reconstruction. We divided the 8 toddler images at 2 years of age into two groups. For T1, the toddler images in the two groups were used to learn dictionaries D1(T1) and D2(T1). These two dictionaries were then used independently for SR reconstruction of the 8 neonatal images. For the first group, using D1(T1) implies that we are performing *intra*-subject SR, whereas using D2(T1) implies *inter*-subject SR. For the second group, the intra- and inter-subject relationships are inverted. This process is repeated for dictionaries constructed using the toddler T2 images, i.e., D1(T2) and D2(T2). Fig. 3 shows SNR/SSIM results given by RSSR2 for the 8 neonatal T1 and T2. It can be observed from the figures that SR performance is almost unaffected whether the dictionary used in SR is from the same subject.

4.4. Age of toddler

We further assess whether SR is affected by the age of the toddler whose image is used for learning the dictionary. RSSR2 was used for SR reconstruction of the first 24 subjects using dictionaries learned from toddler images of the 3 subjects scanned at 5 time points (i.e., 24, 36, 48, 60 and 72 months). Fig. 4 shows box plots of the SNR/SSIM results for T1 and T2 images, respectively. The central line of each box plot is the median. The edges mark the 25th and 75th percentiles, and the whiskers extend to the minimum and the maximum. As can be seen from the figures, the SR performance is relatively unaffected by the actual time point the dictionary is associated with.

4.5. Results for simulated images

We compared the proposed algorithm with the competing methods, including the spline interpolation (Spline) (Lehmann et al., 1999), NLMU (Manjon et al., 2010), LRTV (Shi et al., 2015), and LGSR (Zhang et al., 2018). We used the source codes provided by the authors of the respective methods in

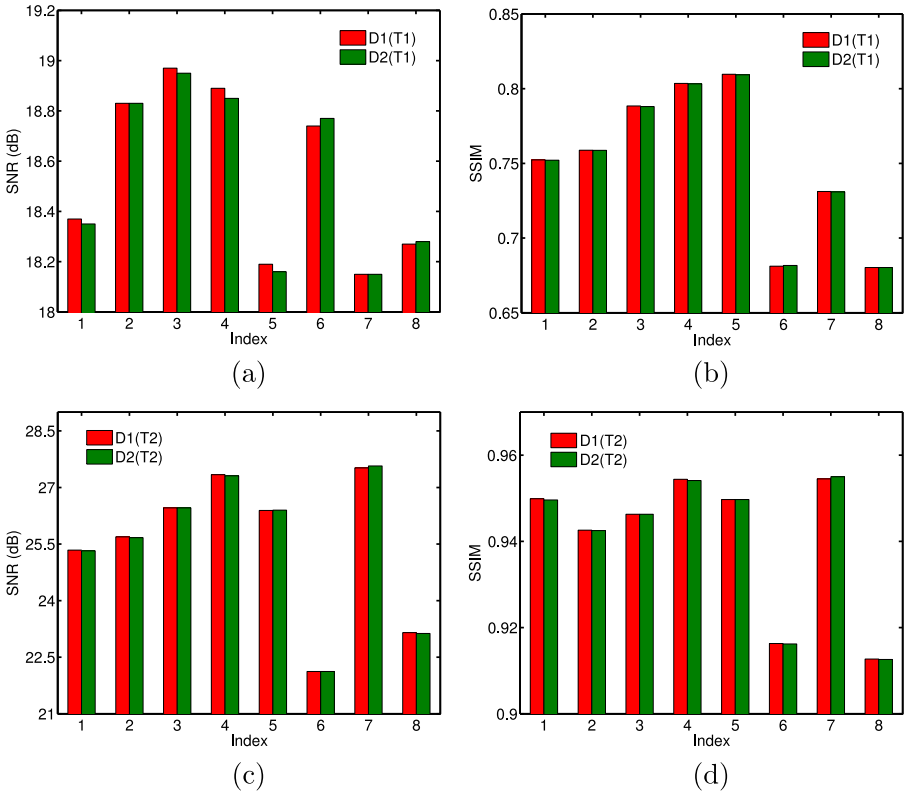

Fig. 3. SNR/SSIM results given by RSSR2 for SR using dictionaries D1 and D2 for the 8 neonatal LR T1/T2 images. From left to right and top to bottom: (a) SNR for T1, (b) SSIM for T1, (c) SNR for T2, and (d) SSIM for T2.

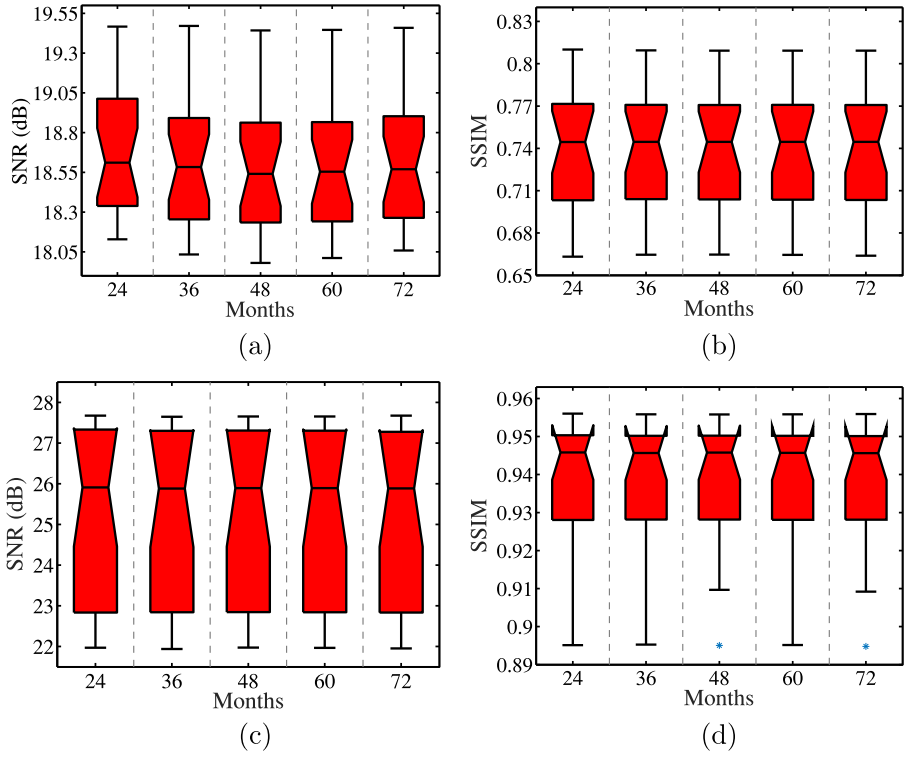

Fig. 4. SR performance for 24 neonatal T1/T2 images over dictionaries learned from images of toddlers scanned at 24, 36, 48, 60, and 72 months. From left to right and top to bottom: (a) SNR for T1, (b) SSIM for T1, (c) SNR for T2, and (d) SSIM for T2.

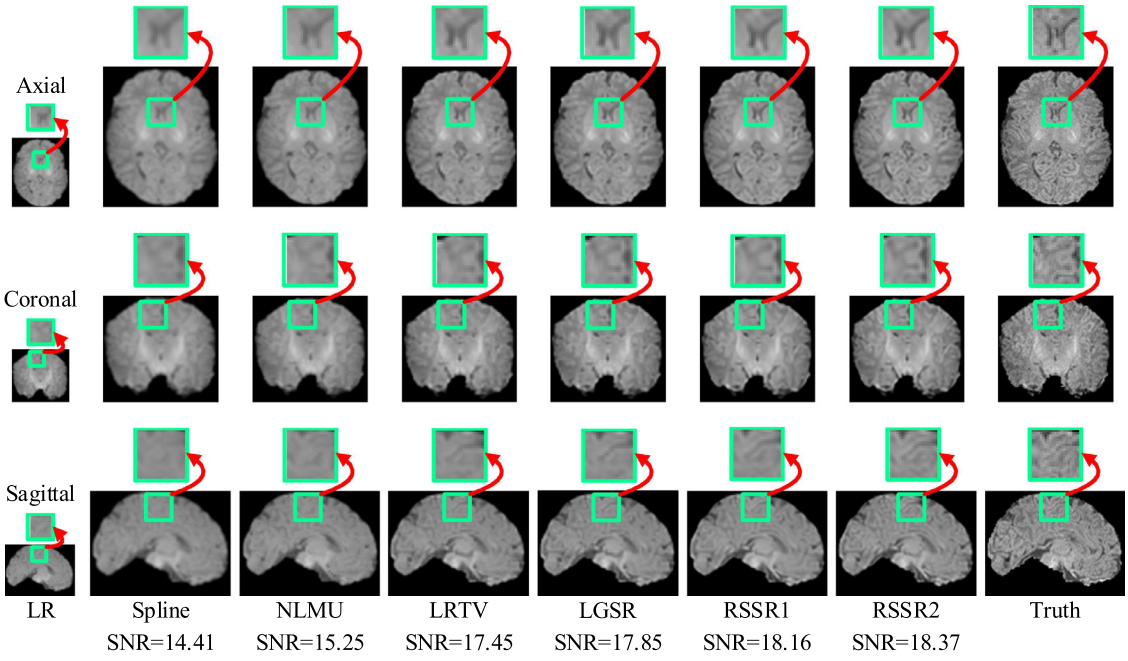

Fig. 5. Visual comparison of axial, coronal and sagittal views of the HR image reconstructed from one simulated LR T1 image.

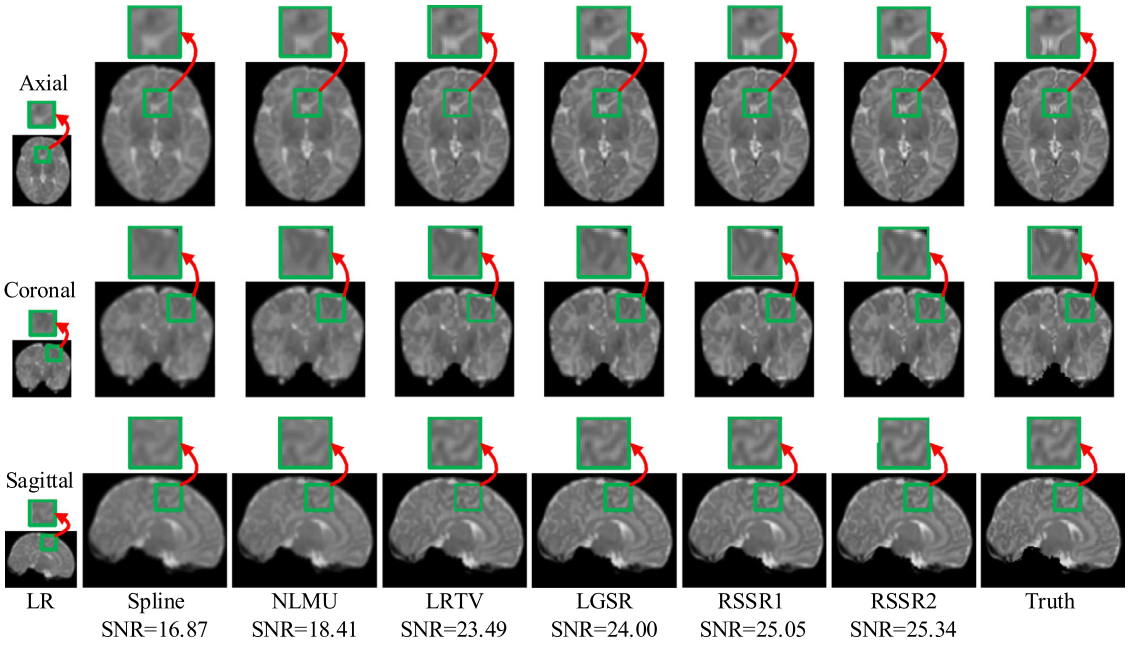

Fig. 6. Visual comparison of axial, coronal and sagittal views of the HR image reconstructed from one simulated LR T2 image.

our evaluation: NLMU (Manjon et al., 2010)[1] and LRTV (Shi et al., 2015).[2] For a fair comparison, we adopted the same Gaussian blur kernel of size $5 \times 5 \times 5$ with a standard deviation of 1 voxel to produce the simulated LR neonatal images and used spline interpolation for the initialization of NLMU (Manjon et al., 2010), LRTV (Shi et al., 2015), LGSR (Zhang et al., 2018) and our methods.

Figs. 5 and 6 provide a visual comparison of the axial, sagittal, and coronal views of a neonatal SR image for a randomly selected subject. We can see from the figures that RSSR2 recovers more anatomical details than RSSR1 and the competing methods.

Fig. 7 shows the SNR/SSIM box plots of the 24 neonatal T1 and T2 SR images. RSSR1 with ℓ_1 norm regularization gives significant improvements over the competing methods both visually and quantitatively. Furthermore, RSSR2 with partly quadratic regularization outperforms RSSR1 in recovering tissue boundaries and gives the best SNR/SSIM and visual quality. The improvements given by RSSR2 over the competing methods are statistically significant with level $\mathcal{P} < 0.0001$ (two sample t-tests).

Considering both kernel width and standard deviation of Gaussian function having an impact on the SR performance, we implemented another experiment to validate the robustness of RSSR2. In this experiment, we chose larger kernel width and standard

[1] Monomodal MRI super-resolution, March 31, 2016, https://sites.google.com/site/pierrickcoupe/.

[2] LRTV for Image Super-Resolution, March 31, 2016, https://bitbucket.org/fengshi421/superresolutiontoolkit.

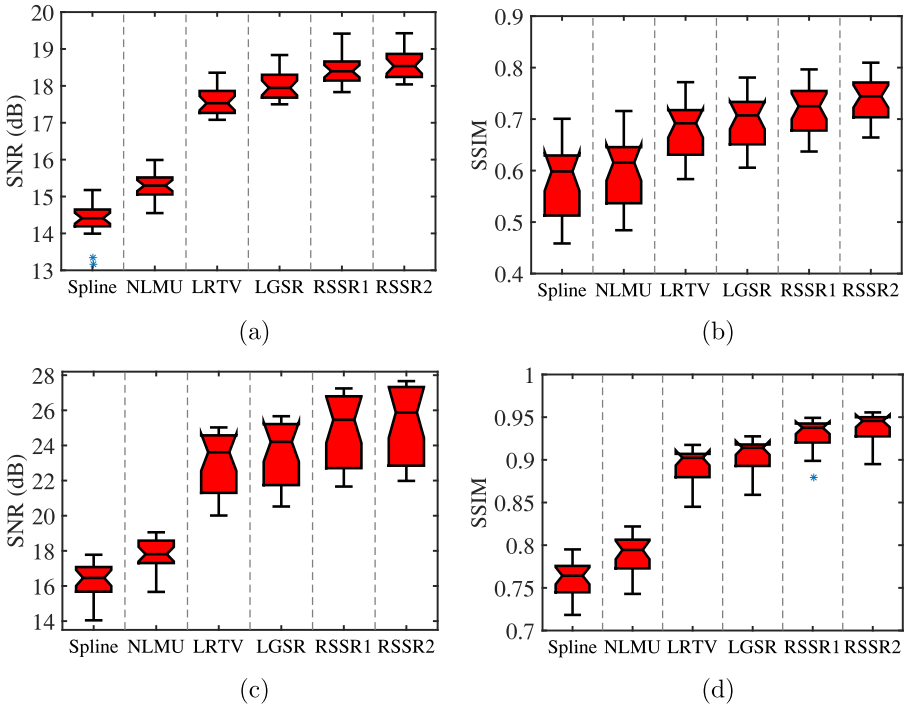

Fig. 7. SNR/SSIM results of 24 reconstructed HR neonatal T1/T2 images. From left to right and top to bottom: (a) SNR for T1, (b) SSIM for T1, (c) SNR for T2, and (d) SSIM for T2.

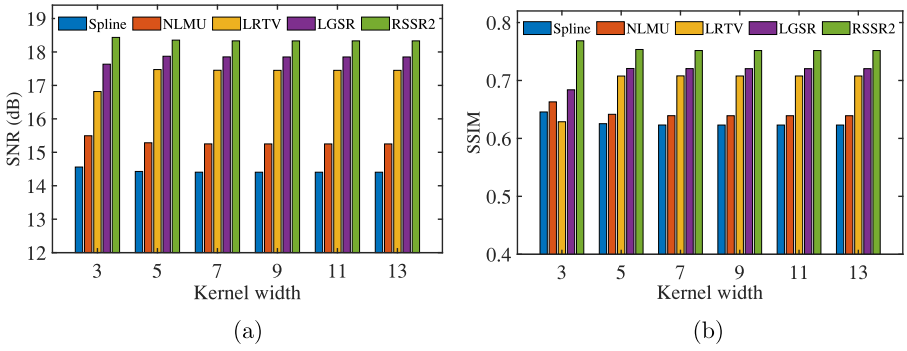

Fig. 8. SNR and SSIM results obtained by the competing method and our RSSR2 with different kernel widths but a fixed standard deviation.

deviation across a wide range to verify the efficacy of RSSR2. For a randomly selected neonate, Fig. 8 provides SNR and SSIM results obtained by the competing method and our RSSR2 with different kernel widths but a fixed standard deviation. From the results, we can see all competing methods and RSSR2 are robust to kernel width. Considering larger standard deviations resulting in more smoothed LR images, we further compared our RSSR2 with the competing methods using different standard deviations but a fixed kernel width, as shown in Fig. 9. From the results, all methods are sensitive to the standard deviations, but our RSSR2 is still able to achieve the best results.

4.6. Results for real images

Figs. 10 and 11 provide the SR results of a random neonate obtained by spline interpolation (Lehmann et al., 1999), NLMU (Manjon et al., 2010), LRTV (Shi et al., 2015), LGSR (Zhang et al., 2018), RSSR1 and RSSR2. Spline interpolation (Lehmann et al., 1999) and NLMU (Manjon et al., 2010) blur the edges in the reconstructed HR images. Although LRTV (Shi et al., 2015) and LGSR (Zhang et al., 2018) can reconstruct HR images with higher contrast, they cannot recover some fine anatomical structures, and cause contrast distortion and smoothing artifacts. RSSR2 gives sharper edges and clearer anatomical structures than RSSR1. RSSR2 also results in fewer artifacts compared with the competing methods.

Table 1
Comparison of computational complexity (in seconds).

Image size	Spline	NLMU	LRTV	LGSR	RSSR2
$128 \times 128 \times 99$	0.34	18.91	5193.51	6710.38	2315.65
$256 \times 256 \times 198$	1.57	98.27	38897.10	48098.64	4565.12

4.7. Computational complexity

Table 1 shows the comparison of computation times between our RSSR2 and the competing methods for two cases: a simulated image of size $128 \times 128 \times 99$ and a real image of size $256 \times 256 \times 198$, indicating that our RSSR2 without code optimization takes longer than Spline (Lehmann et al., 1999) and NLMU (Manjon et al., 2010), but is faster than LRTV (Shi et al., 2015) and LGSR (Zhang et al., 2018). For other images, we obtained

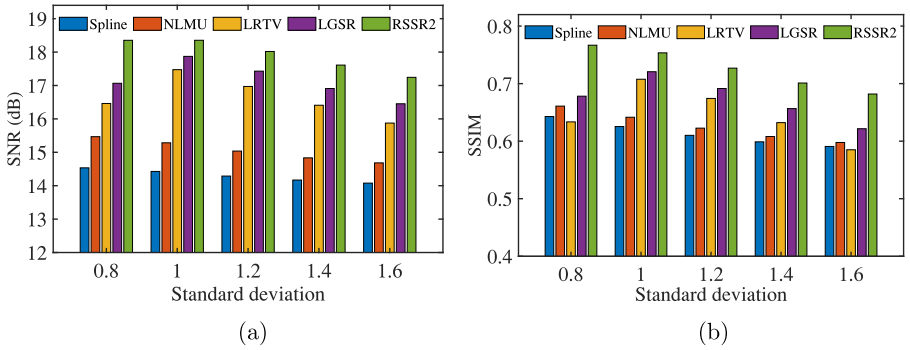

Fig. 9. SNR and SSIM results obtained by the competing methods and our RSSR2 with different standard deviations but a fixed kernel width.

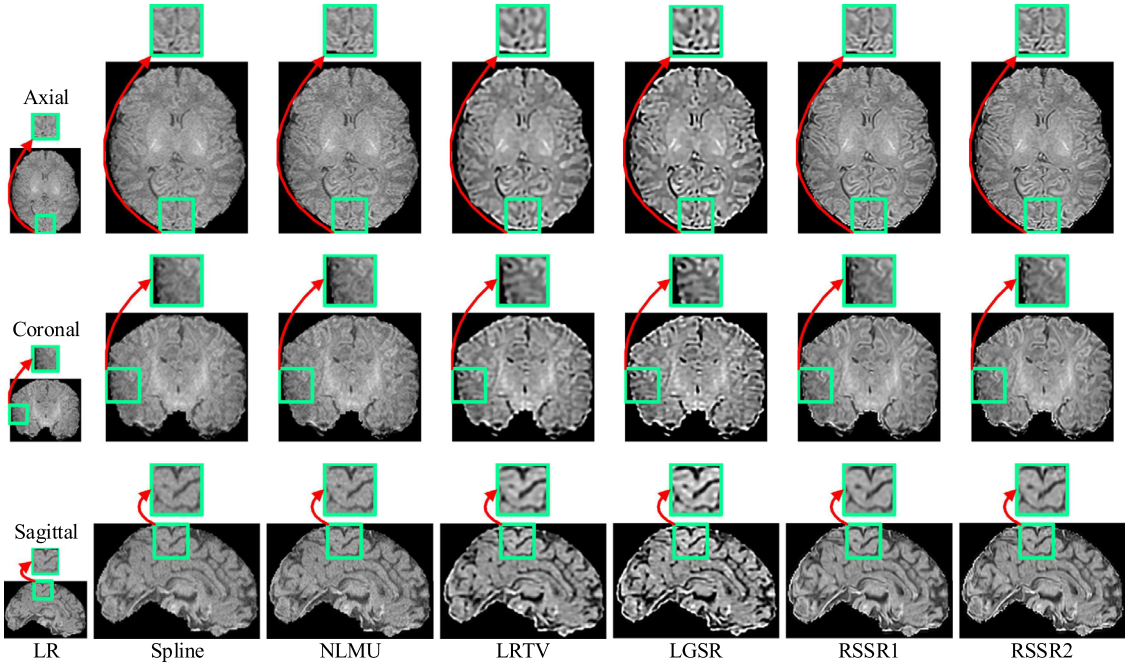

Fig. 10. Visual comparison of axial, coronal and sagittal views of the HR image reconstructed from one real LR T1 image.

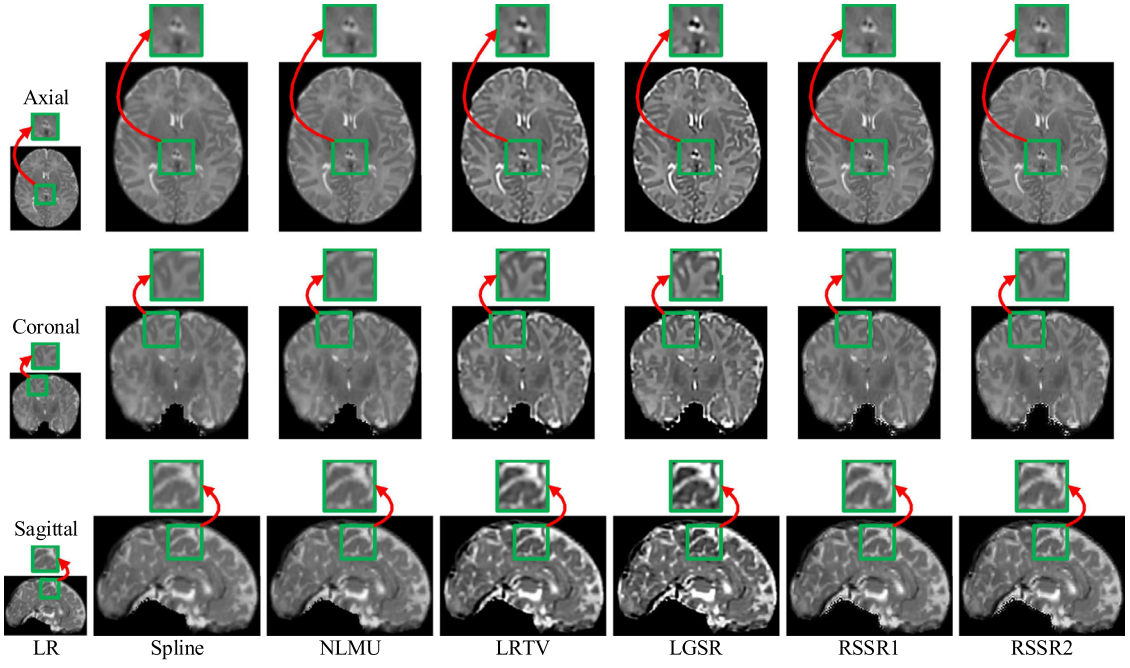

Fig. 11. Visual comparison of axial, coronal and sagittal views of the HR image reconstructed from one real LR T2 image.

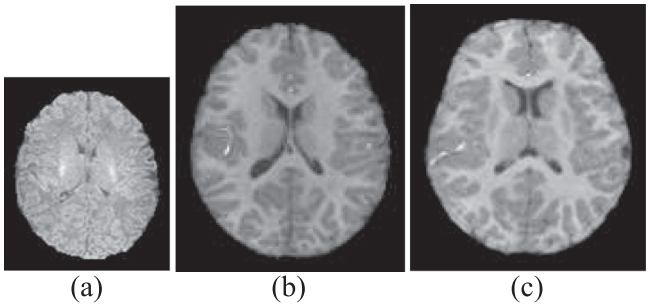

Fig. 12. Comparison of T1 images of (a) a neonate, (b) its toddler counterpart, and (c) another toddler. Both toddlers are 2 years of age.

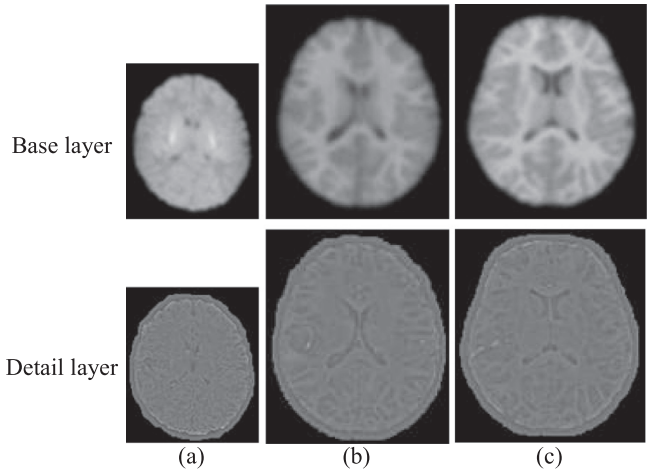

Fig. 13. Base and detail layers of images in Fig. 12.

similar results. All experiments were implemented using Matlab 2018b in CentOS Linux 7.2 operating system on a computer with Intel(R) Xeon(R) CPU E5-2620 v4 @2.10GHz and 64GB RAM.

5. Discussion

5.1. Longitudinal SR – challenges and solutions

In developmental studies, a pediatric subject can be scanned longitudinally at multiple time points. Image contrast changes very rapidly with time, and typically the images closer to the perinatal period exhibit significantly lower quality. Fig. 12 shows the typical differences between neonatal and toddler images. The structural similarity across different time points can be leveraged for SR by imposing a longitudinal prior during SR reconstruction. However, not all subjects are scanned with longitudinal follow-ups. We overcome this problem by borrowing longitudinal information *across* subjects.

Image brightness may vary across time and subjects, even for the same subject. For example, the intensity difference between the neonatal and toddler images is shown in Fig. 12. For the suppression of adverse impact caused by brightness changes, we introduce a two-layer representation by decomposing the image into a base layer and a detail layer (Xiao et al., 2014; Fang et al., 2015). The base layer consists of the smoothed version of the image obtained via Gaussian filtering. The detail layer is the difference between the original image and the base layer. Fig. 13 shows the base and detail layers of the images shown in Fig. 12. From the figure, it can be observed that the brightness of the base layers varies across images. On the other hand, the brightness of the detail layers is consistent. Thus, this two-layer representation ensures the consistence between the detail layers of both neonatal images and toddler images. For this reason, high-frequency details can be borrowed across subjects for SR reconstruction. Fig. 14 shows that patch recurrence, for 8 toddler images, improves in the detail layer compared with the original images, which implies that the detail layers have higher self-similarity.

The proposed method reconstructs the desired HR neonatal images with the aid of high-frequency information learned from toddler images of the same or other subjects. Although the detail layer containing reverse edges is not equal to the actual difference between empirically collected HR and LR images, both of them represent the high-frequency details of HR image in two different ways. Since the self-similarity prior holds for MR images (Buades et al., 2005; Rousseau and Initiative, 2010), there are abundant patches containing similar patterns across images, even though they have the remarkable individual differences in anatomical structures. For neonatal image SR reconstruction, we only need to super-resolve the detail layer by exploiting nonlocal similarity of anatomical structures. The HR neonatal images are accurately estimated by adding the base layer and the super-resolved detail layer. This two-layer representation strategy overcomes the issue of the discrepancies between test and training images, even though they are obtained from different subjects at different time points. The proposed method can reconstructed the HR neonatal images effectively without affecting the image acquisition process.

5.2. Experimental setup and verification

In the experimental setup, as shown in Fig. 2, RSSR2 is robust to the parameters K and N, but very sensitive to other parameters p and ρ. From Fig. 2(a) and (b), as p increases, SNR and SSIM first increases and then decreases for RSSR2, implying that p has an appropriate value to make RSSR2 approximate the best performance. In sparse representation and dictionary learning, too large p cannot adequately express local image patterns, while too small p cannot effectively depict the relevance between voxels in local neighborhoods. On the other hand, when ρ increases, RSSR2 achieves higher SNR and SSIM. As ρ determines the increment of detail layer updating in the iterative solution, RSSR2 is sensitive to ρ for the predefined maximum number of iterations as the convergence condition. Theoretically, RSSR2 is robust to ρ with an appropriate range of values when the number of iterations is large enough. Too small ρ makes RSSR2 converge too slowly, while too large ρ causes algorithm divergence and the worse results due to lack of data fidelity. From Fig. 2(c) and (d), as N increases, more toddler images for dictionary learning result in worse reconstruction because of overfitting in dictionary learning. Theoretically, more toddler images can provide much richer patterns, which is beneficial to the representation ability of learned dictionaries. However, dictionary learning also involves the number K of sub-dictionaries. As K increases, too many toddler images cause overfitting and heavy computation, but too few toddler images induce underfitting and the instability. In parameter setting, we chose $N = 4$ and $K = 1024$ under the balanced trade-off between pattern diversity and the limitations on our computational ability and memory capacity. The optimal selection of K and N will be studied further in the future.

In the experimental verification, we evaluated the proposed method with the upscaling factor 2 on the input neonatal images and the toddler images at the spatial resolution of range about $1 \sim 2$ mm^3. The proposed method works well and can accurately reconstruct the HR neonatal images. The evaluation of the proposed method on test images of other spatial resolution is left as future work. Incidentally, RSSR1 amounts to the 3D version of NCSR (Dong et al., 2013), except that a discrepant external dataset instead of an internal dataset is used for dictionary learning. As an external dataset, toddler images have the discrepancies from neonate images (i.e., test images), which is not solved by existing

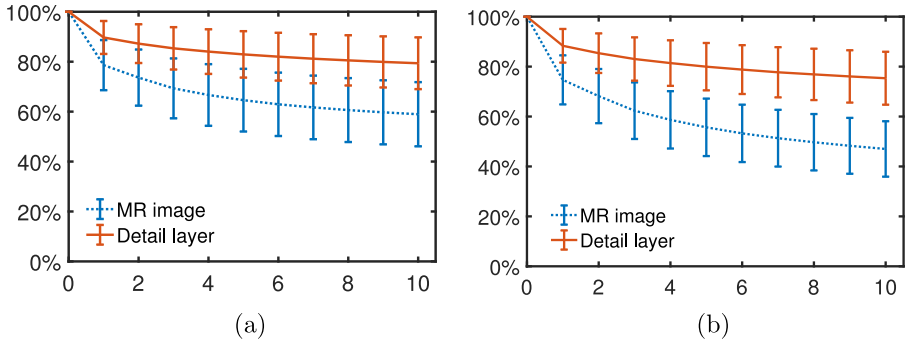

Fig. 14. Recurrence of (a) image patches and (b) edge patches in 8 toddler images based on the original MR images and the detail layers. The horizontal axis shows the minimal number of matching patches. The vertical axis shows the rate of recurrence.

deep learning methods. Since toddler images (i.e., external dataset) have higher quality than neonate images (i.e., internal dataset), our RSSR2 can achieve better results than the competing methods. In fact, our RSSR2 is a generalized form of RSSR1 by extending ℓ_1 norm regularization to partly quadratic penalty regularization. PVE exists in MR images of both adults and pediatric subjects. The common strategy for decreasing PVE is to use smaller-defined voxels for collection of HR neonatal images during the scanning process by choosing a thinner section, a smaller field of view, and/or a larger imaging matrix size. But this strategy leads to lower SNR and longer scan time (or smaller imaging regions). The collected HR neonatal MR images still have perceptible artifacts because of imperfect MRI scanners, even for the same modality of the same subject at a single time point. Due to the lack of ideal HR neonatal MR images as ground truth, we only provided a visual comparison of reconstructed HR images obtained by different methods for the evaluation on real images.

6. Conclusion

In this paper, we have proposed a novel SR method that is based on residual-structured sparse representation with partly quadratic regularization. Our method reconstructs the HR neonatal brain image of one subject with the help of the toddler images of other subjects. We propose a two-layer representation to recover high-frequency components and also to overcome brightness changes across scanners and sites. This provides a solution to the problem of the discrepancies between test and training data. Experimental results indicate that the proposed method is superior, both qualitatively and quantitatively, to state-of-the-art methods.

Acknowledgements

This work was supported in part by NIH grants (MH100217, MH108914), as well as an NIH grant (1U01MH110274) and the efforts of the UNC/UMN Baby Connectome Project Consortium.

Conflict of interest

The authors declare no conflict of interest.

References

Aly, H.A., Dubois, E., 2005. Image up-sampling using total-variation regularization with a new observation model. IEEE Trans. Image Process. 14 (10), 1647–1659.
Bayram, I., 2016. On the convergence of the iterative shrinkage/thresholding algorithm with a weakly convex penalty. IEEE Trans. Signal Process. 64 (6), 1597–1608.
Beck, A., Teboulle, M., 2009. A fast iterative shrinkage-thresholding algorithm for linear inverse problems. SIAM J. Imaging Sci. 2 (1), 183–202.
Bioucas-Dias, J.M., Figueiredo, M.A.T., 2007. A new twist: two-step iterative shrinkage/thresholding algorithms for image restoration. IEEE Trans. Image Process. 16 (12), 2992–3004.
Buades, A., Coll, B., Morel, J.M., 2005. A review of image denoising algorithms, with a new one. Multiscale Model. Simul. 4 (2), 490–530.
Candes, E.J., Wakin, M.B., Boyd, S.P., 2008. Enhancing sparsity by reweighted l(1) minimization. J. Fourier Anal. Appl. 14 (5–6), 877–905.
Chen, Y., Shi, F., Christodoulou, A. G., Xie, Y., Zhou, Z., Li, D., 2018a. Efficient and accurate MRI super-resolution using a generative adversarial network and 3D multi-level densely connected network. arXiv:1803.01417.
Chen, Y., Xie, Y., Zhou, Z., Shi, F., Christodoulou, A.G., Li, D., 2018. Brain MRI super resolution using 3D deep densely connected neural networks. In: IEEE International Symposium on Biomedical Imaging, pp. 739–742.
Dong, C., Loy, C.C., He, K.M., Tang, X.O., 2016. Image super-resolution using deep convolutional networks. IEEE Trans. Pattern Anal. Mach. Intell. 38 (2), 295–307.
Dong, W.S., Zhang, L., Shi, G.M., Li, X., 2013. Nonlocally centralized sparse representation for image restoration. IEEE Trans. Image Process. 22 (4), 1618–1628.
Fang, H., Yi, B., Zhang, Y., Xie, Q., 2015. Tone mapping based on fast image decomposition and multi-layer fusion. IET Comput. Vis. 9 (6), 937–942.
Fattal, R., 2007. Image upsampling via imposed edge statistics. ACM Trans. Graph. 26 (3), 95.
Gao, H.Y., Bruce, A.G., 1997. Waveshrink with firm shrinkage. Stat. Sin. 7 (4).
Gilmore, J.H., Lin, W., Prastawa, M.W., Looney, C.B., Vetsa, Y.S.K., Knickmeyer, R.C., Evans, D.D., Smith, J.K., Hamer, R.M., Lieberman, J.A., Gerig, G., 2007. Regional gray matter growth, sexual dimorphism, and cerebral asymmetry in the neonatal brain. J. Neurosci. 27 (6), 1255–1260.
Hou, B., Zhou, K., Jiao, L.C., 2018. Adaptive super-resolution for remote sensing images based on sparse representation with global joint dictionary model. IEEE Trans. Geosci. Remote Sens. 56 (4), 2312–2327.
Huang, J.J., Siu, W.C., Liu, T.R., 2015. Fast image interpolation via random forests. IEEE Trans. Image Process. 24 (10), 3232–3245.
Jiang, W., Yang, X., Wu, W., Liu, K., Ahmad, A., Sangaiah, A.K., Jeon, G., 2018. Medical images fusion by using weighted least squares filter and sparse representation. Comput. Electr. Eng. 67, 252–266.
Krishnan, D., Fergus, R., 2009. Fast image deconvolution using hyper-Laplacian priors. In: Advances in Neural Information Processing Systems, pp. 1033–1041.
Ledig, C., Theis, L., Huszar, F., Caballero, J., Aitken, A., Tejani, A., Totz, J., Wang, Z., Shi, W., 2017. Photo-realistic single image super-resolution using a generative adversarial network. In: IEEE Conference on Computer Vision and Pattern Recognition, pp. 105–114.
Lehmann, T.M., Gonner, C., Spitzer, K., 1999. Survey: interpolation methods in medical image processing. IEEE Trans. Med. Imaging 18 (11), 1049–1075.
Liu, H.C., Yao, T., Li, R.Z., 2016. Global solutions to folded concave penalized nonconvex learning. Ann. Stat. 44 (2), 629–659.
Lustig, M., Donoho, D.L., Pauly, J.M., 2007. Sparse MRI: the application of compressed sensing for rapid MR imaging. Magn. Reson. Med. 58 (6), 1182–1195.
Lustig, M., Donoho, D.L., Santos, J.M., Pauly, J.M., 2008. Compressed sensing MRI. IEEE Signal Process. Mag. 25 (2), 72–82.
Manjon, J.V., Coupe, P., Buades, A., Fonov, V., Collins, D.L., Robles, M., 2010. Non-local MRI upsampling. Med. Image Anal. 14 (6), 784–792.
Mao, X., Shen, C., Yang, Y., 2016. Image restoration using very deep convolutional encoder-decoder networks with symmetric skip connections. In: Advances in Neural Information Processing Systems, pp. 2802–2810.
Marquina, A., Osher, S.J., 2008. Image super-resolution by TV-regularization and bregman iteration. J. Sci. Comput. 37 (3), 367–382.
Park, T., Casella, G., 2008. The Bayesian lasso. J. Am. Stat. Assoc. 103 (482), 681–686.
Pham, C.H., Ducournau, A., Fablet, R., Rousseau, F., 2017a. Brain MRI super-resolution using deep 3D convolutional networks. In: IEEE International Symposium on Biomedical Imaging, pp. 197–200.
Pham, C.H., Fablet, R., Rousseau, F., 2017b. Multi-scale brain MRI super-resolution using deep 3D convolutional networks.
Rousseau, F., Initiative, T.A.D.N., 2010. A non-local approach for image super-resolution using intermodality priors. Med. Image Anal. 14 (4), 594–605.

Shi, F., Cheng, J., Wang, L., Yap, P.T., Shen, D., 2015. LRTV: MR Image super-resolution with low-rank and total variation regularizations. IEEE Trans. Med. Imaging 34 (12), 2459–2466.
Shi, F., Wang, L., Dai, Y.K., Gilmore, J.H., Lin, W.L., Shen, D.G., 2012. Label: pediatric brain extraction using learning-based meta-algorithm. Neuroimage 62 (3), 1975–1986.
Su, H., Xing, F., Kong, X., Xie, Y., Zhang, S., Yang, L., 2015. Robust cell detection and segmentation in histopathological images using sparse reconstruction and stacked denoising autoencoders. In: MICCAI, pp. 383–390.
Sun, J., Xu, Z.B., Shum, H.Y., 2011. Gradient profile prior and its applications in image super-resolution and enhancement. IEEE Trans. Image Process. 20 (6), 1529–1542.
Tai, Y., Yang, J., Liu, X., 2017. Image super-resolution via deep recursive residual network. In: IEEE Conference on Computer Vision and Pattern Recognition, pp. 1–9.
Tibshirani, R., 1996. Regression shrinkage and selection via the lasso. J. R. Stat. Soc. Ser. B 58 (1), 267–288.
Tuia, D., Flamary, R., Barlaud, M., 2016. Nonconvex regularization in remote sensing. IEEE Trans. Geosci. Remote Sens. 54 (11), 6470–6480.
Wang, Z., Bovik, A.C., Sheikh, H.R., Simoncelli, E.P., 2004. Image quality assessment: from error visibility to structural similarity. IEEE Trans. Image Process. 13 (4), 600–612.
Xiao, J., Li, W., Liu, G., Shaw, S.L., Zhang, Y., 2014. Hierarchical tone mapping based on image colour appearance model. IET Comput. Vis. 8 (4), 358–364.
Yan, Q., Xu, Y., Yang, X.K., Nguyen, T.Q., 2015. Single image superresolution based on gradient profile sharpness. IEEE Trans. Image Process. 24 (10), 3187–3202.
Yang, J.C., Wright, J., Huang, T.S., Ma, Y., 2010. Image super-resolution via sparse representation. IEEE Trans. Image Process. 19 (11), 2861–2873.
Yao, J., Xu, Z., Huang, X., Huang, J., 2018. An efficient algorithm for dynamic MRI using low-rank and total variation regularizations. Med. Image Anal. 44, 14–27.
Yu, G.S., Sapiro, G., Mallat, S., 2012. Solving inverse problems with piecewise linear estimators: from Gaussian mixture models to structured sparsity. IEEE Trans. Image Process. 21 (5), 2481–2499.
Yue, L., Shen, H., Li, J., Yuan, Q., Zhang, H., Zhang, L., 2016. Image super-resolution: the techniques, applications, and future. Signal Process. 128, 389–408.
Zhang, K.B., Gao, X.B., Tao, D.C., Li, X.L., 2012a. Single image super-resolution with non-local means and steering kernel regression. IEEE Trans. Image Process. 21 (11), 4544–4556.
Zhang, S., Zhan, Y., Dewan, M., Huang, J., Metaxas, D.N., Zhou, X.S., 2012b. Towards robust and effective shape modeling: sparse shape composition. Med. Image Anal. 16 (1), 265–277.
Zhang, S., Zhan, Y., Metaxas, D.N., 2012c. Deformable segmentation via sparse representation and dictionary learning. Med. Image Anal. 16 (7), 1385–1396.
Zhang, Y., Shi, F., Cheng, J., Wang, L., Yap, P.T., Shen, D., 2019. Longitudinally guided super-resolution of neonatal brain magnetic resonance images. IEEE Trans. Cybern. 49 (2), 662–674.
Zhang, Y.Q., Liu, J.Y., Li, M.D., Guo, Z.M., 2014. Joint image denoising using adaptive principal component analysis and self-similarity. Inf. Sci. 259, 128–141.
Zhang, Y.Q., Liu, J.Y., Yang, W.H., Guo, Z.M., 2015a. Image super-resolution based on structure-modulated sparse representation. IEEE Trans. Image Process. 24 (9), 2797–2810.
Zhang, Y.Q., Xiao, J.S., Li, S.H., Shi, C.Y., Xie, G.X., 2015b. Learning block-structured incoherent dictionaries for sparse representation. Sci. China Inf. Sci. 58 (10), 1–15.
Zhu, Z., Yao, J., Xu, Z., Huang, J., Zhang, B., 2018. A simple primal-dual algorithm for nuclear norm and total variation regularization. Neurocomputing 289, 1–12.